Phase-field Modeling of Phase Change Phenomena

Yichen Li

Thesis submitted to the Faculty of the
Virginia Polytechnic Institute and State University
in partial fulfillment of the requirements for the degree of

Master of Science
in
Mathematics

Pengtao Yue
Jeffrey T Borggaard
Honghu Liu

May 13, 2020
Blacksburg, Virginia

Keywords: phases-field method, Allen-Cahn equation, heat transfer, phase transition, finite element method

Phase-field Modeling of Phase Change Phenomena

Yichen Li

(ABSTRACT)

The phase-field method has become a popular numerical tool for moving boundary problems in recent years. In this method, the interface is intrinsically diffuse and stores a mixing energy that is equivalent to surface tension. The major advantage of this method is its energy formulation which makes it easy to incorporate different physics. Meanwhile, the energy decay property can be used to guide the design of energy stable numerical schemes.

In this dissertation, we investigate the application of the Allen-Cahn model, a member of the phase-field family, in the simulation of phase change problems. Because phase change is usually accompanied with latent heat, heat transfer also needs to be considered. Firstly, we go through different theoretical aspects of the Allen-Cahn model for nonconserved interfacial dynamics. We derive the equilibrium interface profile and the connection between surface tension and mixing energy. We also discuss the well-known convex splitting algorithm, which is linear and unconditionally energy stable. Secondly, by modifying the free energy functional, we give the Allen-Cahn model for isothermal phase transformation. In particular, we explain how the Gibbs-Thomson effect and the kinetic effect are recovered. Thirdly, we couple the Allen-Chan and heat transfer equations in a way that the whole system has the energy decay property. We also propose a convex-splitting-based numerical scheme that satisfies a similar discrete energy law. The equations are solved by a finite-element method using the deal.ii library. Finally, we present numerical results on the evolution of a liquid drop in isothermal and non-isothermal settings. The numerical results agree well with theoretical analysis.

Phase-field Modeling of Phase Change Phenomena

Yichen Li

(General Audience Abstract)

Phase change phenomena, such as freezing and melting, are ubiquitous in our everyday life. Mathematically, this is a moving boundary problem where the phase front evolves based on the local temperature. The phase change is usually accompanied with the release or absorption of latent heat, which in turn affects the temperature. In this work, we develop a phase-field model, where the phase front is treated as a diffuse interface, to simulate the liquid-solid transition. This model is consistent with the second law of thermodynamics. Our finite-element simulations successfully capture the solidification and melting processes including the interesting phenomenon of recalescence.

Contents

List of Figures

List of Tables

Chapter 1

Introduction

1.1 Background

In recent years, a lot of research on the modeling of phase change phenomena has emerged, such as crystal growth [1–4], solidification [5–8], and melting [9]. It is fascinating that the crystal growth process could show some incredible physical characteristics both in the growth stage and expansion stage. In general, the crystal growth problem is recognized to be anisotropic, which means the properties of the material are dependent on the orientation. We will discuss anisotropy in Section 2.1.

Figure 1.1: Phase Change Phenomena [1]

One major type of phase change phenomena is solidification. It usually involves the formation of complex microstructure. The most recognized shape of solidification structure is the tree-like shape. One good example is the snowflake formed by a single crystal of ice. This process happens when an supercooled water droplet falls through the sky. In a recent study [10],

[1]Picture form Pexels. Free to use or share, even commercially.

a material known as succinonitrile gained great popularity because it can solidify at room temperature from its melt. It has the characteristic of a transparent colorless crystal, which gives us a good opportunity to observe the crystallization process without setting up an extreme-temperature environment. Another important thing to keep in mind is that the crystallization characteristics of this material is essentially no different from many alloys.

Considering a liquid-solid system that undergoes phase transition, the thermophysical properties such as density or heat capacity invariability take different values in different phases. The physical process can be further complicated by liquid motion. There have been different approaches introduced by Beckermann [7, 8] to address the effect of convection on phase transition. In this work, for simplicity, we will not consider convection and assume that whole system has constant density and other thermophysical properties.

1.2 Phase-field Models

In recent years, phase-field models have demonstrated great potential in simulating solidification and microstructure development. For example, the phaese-field method has been applied to dendritic grwoth in a single substance [6], eutectic and peritectic growth [11], and solidification with solute trapping [12]. In a word, the phase-field method has been widely used in the simulation of crystal growth, solidification, and melting problems. A key aspect of the phase-field method is the introduction of an order parameter, also know as the phase-field variable, that distinguishes the different phases. The transition region between the two phases is treated as a diffuse interface instead of a sharp interface, as illustrated in Fig. 1.2. Thus the fluid properties have a smooth variation and the same set of governing equations can be used in the whole domain.

The phase-field model can be achieved by the gradient flow of energy functional $E(\phi)$:

$$\frac{\partial \phi}{\partial t} = \psi \frac{\delta E}{\delta \phi},$$

where ϕ is called the phase-field variable, the variational derivative $\frac{\delta E}{\delta \phi}$ is also known as the chemical potential and ψ is a non-positive operator. Popular phase-field models include the Cahn-Hilliard model for conserved dynamics and the Allen-Cahn model for non-conserved dynamics. The Allen-Cahn model is usually adopted for the phase transition problem. In recent years, phase-field models have been applied to a variety of incompressible two-phase flow problems. The research community has extensively studied numerical algorithms under the framework of finite element, spectral, and finite-difference methods [13, 14].

The phase-field approach eliminates the need to apply matching conditions at an interface, which may be difficult due to the unknown interface location. For example, interface conditions are required to conserve heat and mass between the two phases. Research suggests that phase-field models have many mathematical advantages over conventional methods for

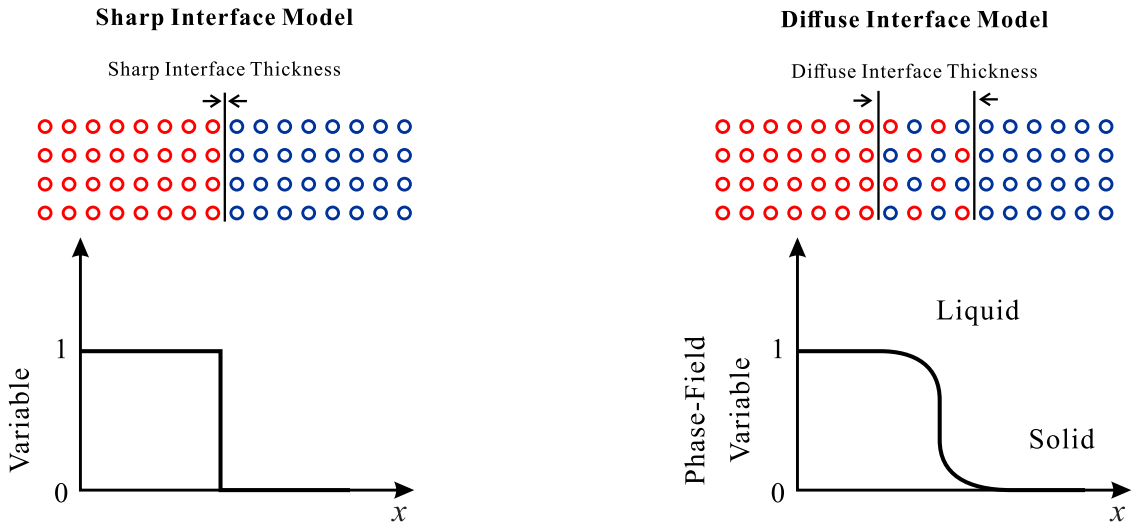

Figure 1.2: Properties are discontinuous at the sharp interface, but vary continuously across the diffuse interface.

moving boundary problems. The energy-based formulation makes it easy to generate reliable results by variational approaches.

The rest of this thesis is organized as follows. In chapter 2, we review the Allen-Cahn equation, its energy law, and the energy-stable convex splitting scheme. We also provide the Allen-Cahn equation for isothermal phase transition. In chapter 3, we develop a coupled system of the Allen-Cahn equation and the heat equation that satisfy an dissipative energy law. We further provide a numerical scheme that honors this energy decay property. In chapter 4, 2D test cases are provided to demonstrate the convergence order of the numerical scheme and to benchmark the Allen-Cahn model. In chapter 5, we present conclusions and future plan.

Chapter 2

Allen-Cahn Equation

2.1 Introduction the Allen-Cahn Equation

The Allen-Cahn equation was first introduced to describe the evolution of phase boundary in the phase change problem in 1979 [15]. It has become popular in many moving interface problems in different areas such as image processing, materials science, biology, and fluid dynamics.

Consider the free energy functional (a.k.a. mixing energy) on domain Ω:

$$E(\phi) = \int F_\phi(\phi, \nabla\phi) d\Omega = \int_\Omega \left[\lambda \left(\frac{1}{2} |\nabla\phi|^2 + f(\phi) \right) \right] d\Omega. \tag{2.1}$$

The Allen-Cahn equation can be expressed as:

$$\frac{\partial \phi}{\partial t} = -M_\phi \mu_\phi = -M_\phi \lambda \left(-\Delta\phi + f(\phi) \right), \tag{2.2}$$

where $\mu_\phi = \frac{\delta E}{\delta \phi}$ is the chemical potential, Δ is the Laplace operator, λ is a parameter that controls the magnitude of mixing energy, and M_ϕ is the mobility parameter. Equation (2.2) is a prototype for the modeling of phase transition. $f(\phi)$ is a double-well potential with two global minima at $\phi = 0$ and 1. In particular, we take $f(\phi) = f_0(\phi)/\epsilon^2$, where $f_0(\phi) = \phi^2(1-\phi)^2$ and ϵ is proportional to the interfacial thickness. The double-well potential $f_0(\phi)$ is shown in Fig. 2.1.

The weak form of the equation (2.2) can be obtained by taking the inner product with a test function v over the domain Ω:

$$(\phi_t, v) - (M_\phi \lambda \Delta\phi, v) + (M_\phi \lambda f(\phi), v) = 0, \tag{2.3}$$

where $(\cdot, \cdot)$ denotes the L^2 inner product on Ω. From integration by parts, we have

$$\int_\Omega M_\phi \lambda \Delta\phi = M_\phi \lambda \int_\Omega \nabla\phi \nabla v - M_\phi \lambda \int_{\partial\Omega} v n \cdot \nabla\phi.$$

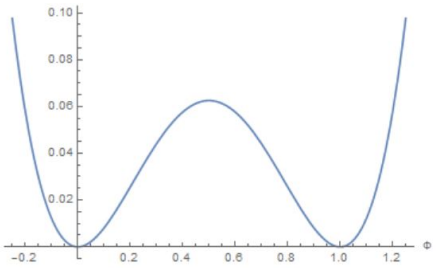

Figure 2.1: The double-well potential $(1-\phi)^2\phi^2$

Thus the weak form becomes

$$(\phi_t, v) - < \mathbf{n} \cdot M_\phi \lambda \nabla\phi, v > + (M_\phi \lambda \nabla\phi, \nabla v) - (M_\phi \lambda f(\phi), v) = 0, \tag{2.4}$$

where $< \cdot, \cdot >$ denotes the inner product on the boundary $\partial\Omega$. After applying the boundary condition $\mathbf{n} \cdot \nabla\phi = 0$, we have the following weak formulation:

$$(\phi_t, v) + (M_\phi \lambda \nabla\phi, \nabla v) - (M_\phi \lambda f(\phi), v) = 0. \tag{2.5}$$

2.1.1 Equilibrium diffuse interface profile

We consider the diffuse interface at equilibrium in 1D. Equation 2.2 reduces to

$$\frac{\delta E}{\delta \phi} = \lambda \left(-\phi_{xx} + \frac{f_0'(\phi)}{\epsilon^2} \right) = 0. \tag{2.6}$$

Suppose the interface is centered at $x = 0$ as shown in Fig. 2.2. In the far field, we have $\phi(-\infty) = 0$, $\phi(\infty) = 1$, $\phi'(-\infty) = \phi'(\infty) = 0$. Multiplying (2.6) by ϕ_x and integrating from $-\infty$ to x, we obtain

$$\frac{1}{2}\phi_x^2 = \frac{f_0(\phi)}{\varepsilon^2}, \tag{2.7}$$

which is equivalent to

$$\phi_x = \frac{\sqrt{2}\phi(1-\phi)}{\varepsilon}. \tag{2.8}$$

Solving (2.8), we arrive at the hyperbolic tangent profile:

$$\phi = \frac{\exp(\frac{x}{\varepsilon/\sqrt{2}})}{1 + \exp(\frac{x}{\varepsilon/\sqrt{2}})} = \frac{1}{2}\left(1 + \tanh\left(\frac{x}{\sqrt{2}\varepsilon}\right)\right). \tag{2.9}$$

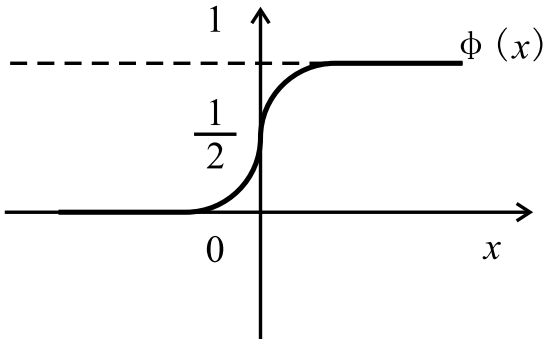

Figure 2.2: Schematic of the equilibrium profile of $\phi(x)$.

2.1.2 Surface tension

In the sharp-interface description, the surface energy is the product of surface tension σ and surface area; in the diffuse-interface description, such energy is replaced by the mixing energy (2.1). Thus the surface tension of a diffuse interface can be obtained by the equivalence of these two energies. For an equilibrium interface in 1D, the surface tension is given by

$$\sigma = \int_{-\infty}^{\infty} \lambda \left(\frac{1}{2}\phi_x^2 + f(\phi) \right) dx. \tag{2.10}$$

Plugging (2.8) and (2.9) into (2.10), we obtain

$$\sigma = \int_{-\infty}^{\infty} \lambda (\phi_x)^2 dx = \frac{1}{3\sqrt{2}} \frac{\lambda}{\varepsilon}, \tag{2.11}$$

which connects σ to λ and ϵ. In practical computations, ϵ is usually chosen based on the mesh size ($\epsilon \gtrsim h$, where h is the mesh size at the inteface), and then λ is assigned to achieve desired σ.

2.1.3 Anisotropic energy

In this subsection, we provide a brief introduction to the free energy for anisotropic solidification. The free energy (2.1) is generalized to

$$E(\phi) = \int_{\Omega} F_\phi(\phi, \nabla\phi) dx. \tag{2.12}$$

We add an anisotropic coefficient $\kappa(\nabla\phi)$ and the energy density F_ϕ becomes

$$F_\phi(\phi, \nabla\phi) = \lambda(\frac{1}{2}|\kappa(\nabla\phi)\nabla\phi|^2 + f(\phi)). \tag{2.13}$$

Here $\kappa(\nabla\phi)$ is a function describing the anisotropic nature of the physical process. For example, in a 2D system, we can choose

$$\kappa(\nabla\phi) = 1 + \tilde{\varepsilon}\cos(m\Theta), \tag{2.14}$$

where m represents the number of fold of anisotropy, $\tilde{\varepsilon}$ represents the strength of anisotropy, and $\Theta = \arctan(\frac{\phi_y}{\phi_x})$ is the orientation angle of the interface. The strong anisotropic coefficient $\kappa(\nabla\phi)$ may induce large numerical oscillations. In this work, we only consider the isotropic case which corresponds to $\tilde{\varepsilon} = 0$ and $\kappa = 1$.

2.2 Temporal discretization by convex splitting

Convex splitting is a simple but robust approach for solving the Allen-Cahn equation. It was originally proposed by Eyre for the Cahn-Hilliard equation [16]. The general idea is that we split the double well potential into the sum of two parts:

$$f(\phi) = f_+(\phi) + f_-(\phi), \tag{2.15}$$

with the f_+ being convex ($f_+''(\phi) \geq 0$) and f_- being concave ($f_-''(\phi) \leq 0$). In particular, we require $f_+'(\phi)$ to be linear and thus $f_-'(\phi) = f'(\phi) - f_+'(\phi)$ is nonlinear. By treating the linear terms implicitly and f_-' explicitly, we arrive at a first-order semi-discrete scheme for the Allen-Cahn equation:

$$\frac{\phi^{n+1} - \phi^n}{\Delta t} = -M_\phi\lambda[-\Delta\phi^{n+1} + f_+'(\phi^{n+1}) + f_-'(\phi^n)]. \tag{2.16}$$

This scheme can be shown to be unconditionally stable.

Theorem 1. *The scheme* (2.16) *with homogeneous boundary condition* $\boldsymbol{n}\cdot\nabla\phi = 0$ *is unconditionally stable with the following discrete energy law:*

$$E^{n+1} - E^n \leq -\frac{1}{M_\phi\Delta t}\|\phi^{n+1} - \phi^n\|^2 - \frac{\lambda}{2}\|\nabla(\phi^{n+1} - \phi^n)\|^2 \leq 0, \tag{2.17}$$

where

$$E^n = \int_\Omega \lambda\left(\frac{1}{2}|\nabla\phi^n|^2 + f(\phi^n)\right)d\Omega.$$

Proof. The energy stability is proved by taking L^2 inner product of equation (2.16) with $-\frac{\phi^{n+1}-\phi^n}{M_\phi}$:

$$-\frac{1}{M_\phi\Delta t}\|\phi^{n+1} - \phi^n\|^2 = \lambda\int_\Omega[-\Delta\phi^{n+1}(\phi^{n+1} - \phi^n) + (f_+'(\phi^{n+1}) + f_-'(\phi^n))(\phi^{n+1} - \phi^n)]d\Omega. \tag{2.18}$$

By integration by parts, the first term in the integrand on the right hand side can be written as

$$\begin{aligned} -(\Delta\phi^{n+1}, \phi^{n+1}-\phi^n) =& -(\boldsymbol{n}\cdot\nabla\phi, \phi^{n+1}-\phi^n)_{\partial\Omega} + (\nabla\phi^{n+1}, \nabla\phi^{n+1}-\nabla\phi^n) \\ =& \frac{1}{2}\left[||\nabla\phi^{n+1}-\nabla\phi^n||^2 + ||\nabla\phi^{n+1}||^2 - ||\nabla\phi||^2\right]. \end{aligned} \tag{2.19}$$

Here we have used the homogeneous boundary condition $\boldsymbol{n}\cdot\nabla\phi = 0$ and the equality $a(a-b) = \frac{1}{2}[(a-b)^2 + a^2 - b^2]$. For the second term in the integrand, we note the following relations from the Taylor series expansions of $f_+'(\phi^{n+1})$ and $f_-'(\phi^n)$:

$$\begin{cases} f_+'(\phi^{n+1})(\phi^{n+1}-\phi^n) = f_+(\phi^{n+1}) - f_+(\phi^n) + \dfrac{1}{2}f_+''(\eta_+)(\phi^{n+1}-\phi^n)^2, \\ \\ f_-'(\phi^n)(\phi^{n+1}-\phi^n) = f_-(\phi^{n+1}) - f_-(\phi^n) - \dfrac{1}{2}f_-''(\eta_-)(\phi^{n+1}-\phi^n)^2, \end{cases} \tag{2.20}$$

where $\eta_+, \eta_- \in (\phi^n, \phi^{n+1})$. Applying equation (2.19) and (2.20) to equation (2.18) we get:

$$\begin{aligned} -\frac{1}{\Delta t}\frac{1}{M_\phi}||\phi^{n+1}-\phi^n||^2 =& \lambda\frac{1}{2}\left[||\nabla\phi^{n+1}-\nabla\phi^n||^2 + ||\nabla\phi^{n+1}||^2 - ||\nabla\phi||^2\right] \\ &+ \lambda\int_\Omega\left[f(\phi^{n+1}) - f(\phi) + \frac{1}{2}(f_+''(\eta) - f_-''(\eta))(\phi^{n+1}-\phi^n)^2\right]d\Omega. \\ =& E^{n+1} - E^n + \lambda\frac{1}{2}||\nabla\phi^{n+1}-\nabla\phi^n||^2 + \lambda\int_\Omega\frac{1}{2}(f_+''(\eta_+) - f_-''(\eta_-))(\phi^{n+1}-\phi^n)^2 d\Omega. \end{aligned} \tag{2.21}$$

After rearranging this equation, we get:

$$\begin{aligned} E^{n+1} - E^n =& -\frac{1}{\Delta t}\frac{1}{M_\phi}||\phi^{n+1}-\phi^n||^2 - \lambda\frac{1}{2}||\nabla\phi^{n+1}-\nabla\phi^n||^2 \\ &- \lambda\int_\Omega\frac{1}{2}\underbrace{(f_+''(\eta_+) - f_-''(\eta_-))}_{part\ A}\underbrace{(\phi^{n+1}-\phi^n)^2}_{part\ B}d\Omega. \end{aligned} \tag{2.22}$$

It is obvious that part A is non-negative because of the assumption $f_+'' \geq 0 \geq f_-''$. We thus get (2.17). □

The current double-well potential $f(\phi) = \frac{f_0}{\varepsilon^2}$ does not have bounded f'' as $\phi \to \pm\infty$. We thus need to modify f (or equivalently f_0) so that we can perform splitting (2.15) [17]:

$$f_0(\phi) = \begin{cases} \phi^2 & \phi < 0 \\ \phi^2(1-\phi)^2 & \phi \in [0,1] \\ (\phi-1)^2 & \phi > 1 \end{cases}.$$

For convenience, we still use same notations f_0 and f. This leads to

$$f_0'(\phi) = \begin{cases} 2\phi & \phi < 0 \\ 2\phi(1-\phi)^2 - 2\phi^2(1-\phi) & \phi \in [0,1] \\ 2(\phi-1) & \phi > 1 \end{cases}.$$

and

$$f_0''(\phi) = \begin{cases} 2 & \phi < 0 \\ 12\phi^2 - 12\phi + 2 & \phi \in [0,1] \\ 2 & \phi > 1 \end{cases}.$$

It is obvious that $f_0''(\phi) \leq 2$.Then we can introduce the splitting with the following convex and concave parts:

$$f_+(\phi) = \frac{\alpha}{2}\frac{\phi^2}{\varepsilon^2}, \quad f_-(\phi) = f(\phi) - \frac{\alpha}{2}\frac{\phi^2}{\varepsilon^2},$$

where $\alpha \geq \max f_0''(\phi) = 2$. It is obvious that $f_+'' > 0$, $f_-'' < 0$, and f_+' is linear.

In the following, we derive the weak form of (2.16). By applying test function $\tilde{\phi}$, we obtain

$$\begin{aligned} \left(\frac{\phi^{n+1}-\phi^n}{\Delta t}, \tilde{\phi}\right) = &\left(M_\phi \lambda \Delta \phi^{n+1}, \tilde{\phi}\right) - \left(M_\phi \lambda \frac{f_0'(\phi^n)}{\varepsilon^2}, \tilde{\phi}\right) \\ &- \left(\frac{M_\phi \lambda \alpha}{\varepsilon^2}(\phi^{n+1}-\phi^n), \tilde{\phi}\right). \end{aligned} \tag{2.23}$$

By integration by parts, the first term on the RHS can be written as

$$\begin{aligned} \int_\Omega M_\phi \lambda \Delta \phi^{n+1} \tilde{\phi} d\Omega &= - M_\phi \lambda \int_\Omega \nabla \phi^{n+1} \cdot \nabla \tilde{\phi} d\Omega + M_\phi \lambda \int_{\partial\Omega} \tilde{\phi} \boldsymbol{n} \cdot \nabla \phi^{n+1} dS \\ &= - M_\phi \lambda \int_\Omega \nabla \phi^{n+1} \cdot \nabla \tilde{\phi} d\Omega, \end{aligned} \tag{2.24}$$

where we have used the homogeneous Neumann boundary condition $\boldsymbol{n} \cdot \nabla \phi = 0$. The final weak form thus reads

$$\begin{aligned} \left(\frac{\phi^{n+1}-\phi^n}{\Delta t}, \tilde{\phi}\right) = &- \left(M_\phi \lambda \nabla \phi^{n+1}, \nabla \tilde{\phi}\right) - \left(M_\phi \lambda \frac{f_0'(\phi^n)}{\varepsilon^2}, \tilde{\phi}\right) \\ &- \left(\frac{M_\phi \lambda \alpha}{\varepsilon^2}(\phi^{n+1}-\phi^n), \tilde{\phi}\right). \end{aligned} \tag{2.25}$$

The weak formulation (2.25) can be rewritten as the following linear system in deal ii by plugging in $\phi_h = \sum_j U_j \phi_j$:

$$AU = F, \tag{2.26}$$

where the components of the matrix A and the right hand side vector F are defined as

$$A^{ij} = \int_\Omega \frac{\phi_i \phi_j}{\Delta t} d\Omega + \int_\Omega M_\phi \lambda \nabla \phi_i \cdot \nabla \phi_j d\Omega + \int_\Omega \frac{M_\phi \lambda \alpha}{\varepsilon^2} \phi_i \phi_j d\Omega, \tag{2.27}$$

and

$$F_i = \int_\Omega \frac{\phi_h^n}{\Delta t} \phi_i d\Omega - \int_\Omega M_\phi \lambda \frac{f_0(\phi_h^n)}{\varepsilon^2} \phi_i d\Omega + \int_\Omega \frac{M_\phi \lambda \alpha}{\varepsilon^2} \phi_h^n \phi_i d\Omega. \tag{2.28}$$

2.3 Allen-Cahn equation for isothermal phase transition

We consider the solid-liquid phase transition with $\phi = 1$ in the liquid phase and $\phi = 0$ in the solid phase. The Allen-Cahn equation can be used to model isothermal phase transition by adopting a new free energy

$$\tilde{E}(\phi, T) = \int_\Omega [F_\phi(\phi, \nabla\phi) + F_T(T, \phi)] d\Omega, \tag{2.29}$$

where F_ϕ is the standard mixing energy density and F_T is the additional term that accounts for the Gibbs-Thompson and kinetic effects of solidification. Following [18, 19], F_T reads

$$F_T(T, \phi) = L\frac{T_M - T}{T_M} q(\phi), \tag{2.30}$$

where L is the latent heat per unit volume, and T_M is the melting temperature, and $q(\phi)$ is some smooth function satisfying $q(0) = 0$, $q(1) = 1$, and $q'(0) = q'(1) = 0$. Different forms of $q(\phi)$ have been used in the literature [6, 20–22], and we take the Hermite interpolant $q(\phi) = \phi^2(3 - 2\phi)$.

According the information given above, the total free energy is given by

$$\tilde{E} = \int_\Omega \left[\lambda\left(\frac{1}{2}|\nabla\phi|^2 + \frac{f_0(\phi)}{\varepsilon^2}\right) + L\frac{T_M - T}{T_M} q(\phi) \right] d\Omega. \tag{2.31}$$

This leads to the chemical potential

$$\frac{\delta\tilde{E}}{\delta\phi} = \mu_\phi + L\frac{T_M - T}{T_M} q'(\phi). \tag{2.32}$$

where $\mu_\phi = \lambda\left(-\Delta\phi + f'(\phi)\right)$. The Allen-Cahn equation thus reads

$$\frac{\partial\phi}{\partial t} = -M_\phi \frac{\delta\tilde{E}}{\delta\phi} = -M_\phi \left[\mu_\phi + L\frac{T_M - T}{T_M} q'(\phi) \right]. \tag{2.33}$$

In the following, we will discuss how the Gibbs-Thomson effect and the kinetic effect are recovered in the Allen-Cahn equation above.

2.3.1 Gibbs-Thomson Effect

In physics, the melting temperature can be modified by the surface energy if the surface curvature is high, which is known as the Gibbs–Thomson effect. From an energetic point of view, a circular interface tends to shrink due to surface tension, which makes the expansion

more difficult. If the drop phase is solid, then we have to lower the temperature below T_M to expand the drop (i.e., to trigger solidification). If the drop phase is liquid, we have to raise the temperature above T_M to expand the drop (i.e., to trigger melting).

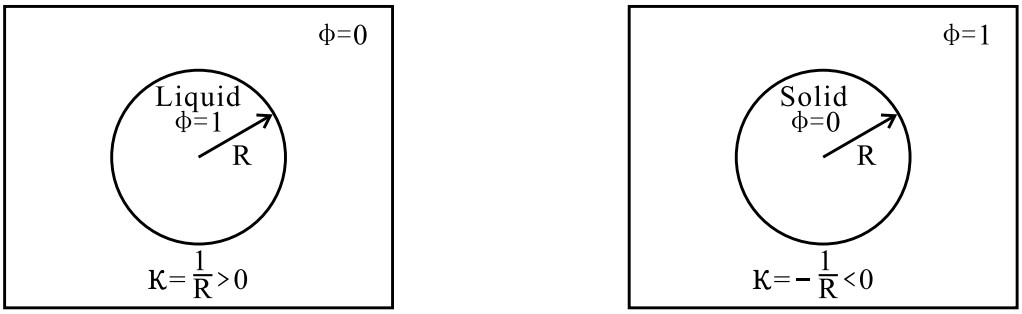

Figure 2.3: $\kappa > 0$ if $\nabla\phi$ is pointing inward and $\kappa < 0$ is $\nabla\phi$ is pointing outward.

Suppose the interface with radius R is stationary (i.e., $\frac{\partial\phi}{\partial t} = 0$) at temperature T_R. Then (2.33) gives

$$\mu_\phi + L\frac{T_M - T_R}{T_M}q'(\phi) = 0. \tag{2.34}$$

Based on the results of the phase-field model for interfacial flows [23], the forcing term due to surface tension can be written as $\mu_\phi\nabla\phi$. By the continuum surface force model [24], the same forcing term reads $\sigma\kappa\nabla\phi$. We thus come up with the relation

$$\mu_\phi = \sigma\kappa, \tag{2.35}$$

where κ is the interface curvature with the sign defined in Fig. 2.3.

Plugging (2.35) into (2.34) and integrating over $\phi \in [0, 1]$, we arrive at

$$T_R = T_M + \frac{\sigma T_M \kappa}{L}, \tag{2.36}$$

which is exactly the relation for the Gibbs-Thomson effect. When the drop phase is liquid, we have $\kappa > 0$ and thus $T_R > T_M$.

2.3.2 Kinetic Effect

Here we consider the propagation of the interface at a given temperature T. Equation (2.33) can be written as

$$\begin{aligned}\frac{\partial \phi}{\partial t} &= -M\left(\mu_\phi + L\frac{T_M - T}{T_M}q'(\phi)\right)\\ &= -M\left(\mu_\phi + L\frac{T_M - T_R}{T_M}q'(\phi) + L\frac{T_R - T}{T_M}q'(\phi)\right)\\ &= -ML\frac{T_R - T}{T_M}q'(\phi),\end{aligned} \tag{2.37}$$

where we have used (2.34) in the third equality.

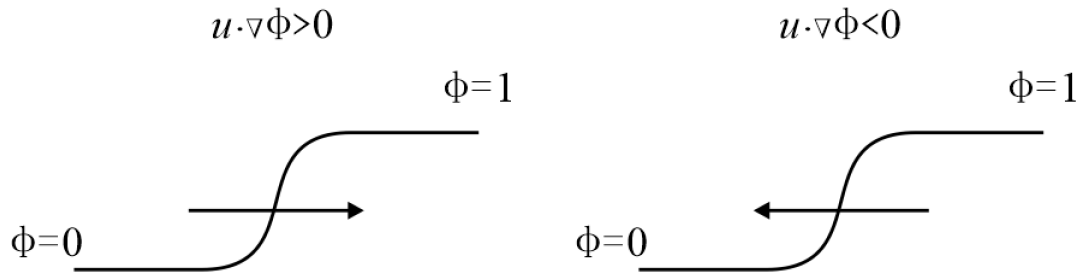

Figure 2.4: $u > 0$ if the interface is propagating toward $\phi = 1$ and $u < 0$ if otherwise.

Suppose ϕ remains its hyperbolic tangent profile (2.9) as the interface propagates with a normal velocity u. The sign of u is defined in Fig. 2.4. Then in the normal direction to the interface, we have

$$\frac{d\phi}{dt} = \frac{\partial \phi}{\partial t} + u\frac{\partial \phi}{\partial x} = 0. \tag{2.38}$$

Combining (2.8), (2.37), and (2.38), we find the velocity of the interface:

$$u = \mu_k\left(T_M - T + T_M\frac{\sigma\kappa}{L}\right), \tag{2.39}$$

where $\mu_k = \frac{3\sqrt{2}\varepsilon ML}{T_M}$ is the kinetic mobility.

Chapter 3

Coupled Allen-Cahn and Heat Equations

Phase change is usually accompanied with the release or absorption of latent heat. This alters the temperature of the phase front and in turn affects phase change. Thus the heat equation for the temperature field needs to be considered to faithfully describe the whole phase change process. In this chapter, we consider a coupled system of the Allen-Cahn equation and the heat equation for the liquid-solid phase change.

3.1 Governing Equations and Energy Law

Based on the total energy that includes the free energy (2.29) and the total enthalpy, we can get the following governing equations from a variational procedure:

$$\frac{\partial \phi}{\partial t} = -M_\phi \left[\lambda \left(-\Delta \phi + f'(\phi) \right) + L \frac{T_M - T}{T_M} q'(\phi) \right], \tag{3.1}$$

$$\frac{\partial}{\partial t} \left[C_p (T - T_M) + L\phi \right] = \nabla \cdot (k \nabla T) - L \frac{T_M - T}{T_M} q'(\phi) \frac{\partial \phi}{\partial t}, \tag{3.2}$$

where C_p is the heat capacity per unit volume and k is the heat conductivity. For simplicity, we assume that C_p and k are both constants. It should be noted that (3.1) is identical to (2.33). In the heat equation (3.2), we have neglected the heat production due to the dissipation in the Allen-Cahn equation. The last term in (3.2) is new and it is added to cancel out the corresponding term in (3.1).

Multiplying (3.1) by $\frac{\partial \phi}{\partial t}$ and integrate over the whole computational domain Ω, we obtain

$$\begin{aligned}
-\frac{1}{M_\phi}\left(\frac{\partial \phi}{\partial t}, \frac{\partial \phi}{\partial t}\right) &= \left(\frac{\partial F_\phi}{\partial \phi} - \nabla \cdot \frac{\partial F_\phi}{\partial \nabla \phi}, \frac{\partial \phi}{\partial t}\right) + \left(L\frac{T_M - T}{T_M} q'(\phi), \frac{\partial \phi}{\partial t}\right) \\
&= \left(\frac{\partial F_\phi}{\partial \phi}\frac{\partial \phi}{\partial t} + \frac{\partial F_\phi}{\partial \nabla \phi} \cdot \frac{\nabla \partial \phi}{\partial t} - \nabla \cdot \left(\frac{\partial F_\phi}{\partial \nabla \phi}\frac{\partial \phi}{\partial t}\right), 1\right) + \left(L\frac{T_M - T}{T_M} q'(\phi), \frac{\partial \phi}{\partial t}\right) \\
&= \left(\frac{\partial F_\phi}{\partial t}, 1\right) + \left(L\frac{T_M - T}{T_M} q'(\phi), \frac{\partial \phi}{\partial t}\right),
\end{aligned} \tag{3.3}$$

where we have used boundary condition $\boldsymbol{n} \cdot \frac{\partial F_\phi}{\partial \nabla \phi} = 0$ in the third equality. Combining this equation with the integration of (3.2) over Ω, we get the energy law

$$\begin{aligned}
\frac{\partial}{\partial t}\int_\Omega \left[F_\phi + h\right] d\Omega &= \int_{\partial\Omega} \nabla \cdot (k \nabla T) d\Omega - \frac{1}{M_\phi}\int_\Omega \left|\frac{\partial \phi}{\partial t}\right|^2 d\Omega \\
&= -\frac{1}{M_\phi}\left\|\frac{\partial \phi}{\partial t}\right\|^2 d\Omega \le 0,
\end{aligned} \tag{3.4}$$

where $h = C_p(T - T_M) + L\phi$ is the enthalpy per unit volume of the solid-liquid mixture and we have used the adiabatic boundary condition $\boldsymbol{n} \cdot \nabla T = 0$ in the second equality. Thus the total energy keeps decreasing in time. It should be noted that this energy will remain constant if we keep the heat production due to Allen-Chan dissipation in (3.2).

3.2 Convex Splitting and Discrete Energy Law

In order to solve unknown term at $n+1$ time level, we keep all unknowns on the left hand side and move others to the right. The stabilized semi-implicit equation (2.25) becomes

$$\begin{aligned}
&\left(\frac{\phi^{n+1}}{\Delta t}, \tilde{\phi}\right) + \left(M_\phi \lambda \nabla \phi^{n+1}, \nabla \tilde{\phi}\right) + \left(\frac{M_\phi \lambda \alpha}{\varepsilon^2}\phi^{n+1}, \tilde{\phi}\right) \\
&\qquad = \left(\frac{\phi^n}{\Delta t}, \tilde{\phi}\right) - \left(M_\phi \lambda f(\phi^n), \tilde{\phi}\right) + \left(\frac{M_\phi \lambda \alpha}{\varepsilon^2}\phi^n, \tilde{\phi}\right) + \left(LM_\phi \frac{T_M - T^n}{T_M} q'(\phi^n), \tilde{\phi}\right).
\end{aligned} \tag{3.5}$$

Now let us consider the heat equation. Using the backward Euler for time discretization, the heat equation becomes

$$\begin{aligned}
&C_p \frac{(T^{n+1} - T^n)}{\Delta t} + L\left(\frac{\phi^{n+1} - \phi^n}{\Delta t}\right) \\
&\qquad = \nabla \cdot (k \nabla (T^{n+1} - T_M)) - L\frac{T^n - T_M}{T_M} q'(\phi^n)\left(\frac{\phi^{n+1} - \phi^n}{\Delta t}\right).
\end{aligned} \tag{3.6}$$

Applying the test function $\tilde{T}$ to equation (3.6), we get

$$\left(C_p\frac{T^{n+1}-T^n}{\Delta t},\tilde{T}\right)+\left(L\frac{\phi^{n+1}-\phi^n}{\Delta t},\tilde{T}\right) = \left(\nabla\cdot(k\nabla(T^{n+1}-T_M)),\tilde{T}\right)-\left(L\frac{T^n-T_M}{T_M}q'(\phi^n)\frac{\phi^{n+1}-\phi^n}{\Delta t},\tilde{T}\right). \quad (3.7)$$

Performing integration by parts, the first term on the right hand side of equation (3.7) becomes

$$\begin{aligned}&\int_\Omega \nabla\cdot(k\nabla(T^{n+1}-T_M))\tilde{T}d\Omega\\ =&k\int_\Omega \Delta((T^{n+1}-T_M))\tilde{T}d\Omega\\ =&-k\int_\Omega \nabla((T^{n+1}-T_M))\cdot\nabla\tilde{T}d\Omega+k\int_{\partial\Omega}\tilde{T}\boldsymbol{n}\cdot\nabla(T^{n+1}-T_M)dS\\ =&-k\int_\Omega \nabla((T^{n+1}-T_M))\cdot\nabla\tilde{T}d\Omega,\end{aligned} \quad (3.8)$$

where we have plugged in the adiabatic condition $\boldsymbol{n}\cdot\nabla T=0$. The semi-discrete weak form of the heat equation (3.2) can be written as

$$\left(C_p\frac{T^{n+1}-T^n}{\Delta t},\tilde{T}\right)+\left(L\frac{\phi^{n+1}-\phi^n}{\Delta t},\tilde{T}\right) = -\left(k\left(\nabla(T^{n+1}-T_M)\right),\nabla\tilde{T}\right)-\left(L\frac{T^n-T_M}{T_M}q'(\phi^n)\frac{\phi^{n+1}-\phi^n}{\Delta t},\tilde{T}\right). \quad (3.9)$$

If we keep all unknown terms to the left and others to the right, then the weak form becomes

$$\left(C_p\frac{T^{n+1}}{\Delta t},\tilde{T}\right)+\left(k\left(\nabla(T^{n+1}-T_M)\right),\nabla\tilde{T}\right) = \left(C_p\frac{T^n}{\Delta t},\tilde{T}\right)-\left(L\frac{\phi^{n+1}-\phi^n}{\Delta t},\tilde{T}\right)-\left(L\frac{T^n-T_M}{T_M}q'(\phi^n)\frac{\phi^{n+1}-\phi^n}{\Delta t},\tilde{T}\right). \quad (3.10)$$

In every time step, we first solve a linear system for (3.5) to get ϕ^{n+1} and then solve a linear system for (3.10) to get T^{n+1}. This scheme can be proven to satisfy the following energy law.

Theorem 2. *The scheme* (3.5) *and* (3.10) *with homogeneous natural boundary conditions satisfy the discrete energy law*

$$(E^{n+1}+H^{n+1})-(E^n+H^n)\le-\frac{1}{M_\phi\Delta t}\|\phi^{n+1}-\phi^n\|^2-\frac{\lambda}{2}\|\nabla(\phi^{n+1}-\phi^n)\|^2\le 0, \quad (3.11)$$

if $f(\phi)$ *is given by extended formula* (2.2) *and* $\alpha\ge 2$, *where* $E^n=\int_\Omega\lambda\left(\frac{1}{2}|\nabla\phi^n|^2+f(\phi^n)\right)d\Omega$ *and* $H^n=\int_\Omega[C_p(T^n-T_M)+L\phi^n]d\Omega$.

Proof. By Taylor expansion, we have

$$f_0'(\phi^n)(\phi^{n+1}-\phi^n) = f_0(\phi^{n+1}) - f_0(\phi^n) - \frac{1}{2}f_0''(\eta)(\phi^{n+1}-\phi^n)^2, \tag{3.12}$$

where $\eta \in (\phi^n, \phi^{n+1})$.

Then by taking the test function $\tilde{\phi} = -\frac{\phi^{n+1}-\phi^n}{M_\phi}$ in (3.5) and following a similar procedure as the proof of Theorem 1, we get

$$\begin{aligned} E^{n+1} - E^n =& -\frac{1}{\Delta t}\frac{1}{M_\phi}\|\phi^{n+1}-\phi^n\|^2 - \lambda\int_\Omega\left[\frac{1}{2}\left(\alpha - \frac{f_0''(\eta)}{\varepsilon^2}\right)(\phi^{n+1}-\phi^n)^2 + \frac{1}{2}\|\nabla\phi^{n+1}-\nabla\phi^n\|^2\right]d\Omega \\ &+ \int_\Omega L\frac{\tilde{T}^*}{T_M}q'(\phi^*)(\phi^{n+1}-\phi^n)d\Omega \\ \le& -\frac{1}{M_\phi\Delta t}\|\phi^{n+1}-\phi^n\|^2 - \frac{\lambda}{2}\|\nabla(\phi^{n+1}-\phi^n)\|^2 + \int_\Omega L\frac{T^n-T_M}{T_M}q'(\phi^n)(\phi^{n+1}-\phi^n)d\Omega, \end{aligned} \tag{3.13}$$

where we have used $\alpha \ge f_0''(\eta)$.

By taking the test function $\tilde{T} = 1$, (3.10) gives

$$\left(C_p(T^{n+1}-T_M) + L\phi^{n+1}, 1\right) - \left(C_p(T^n-T_M) + L\phi^n, 1\right) = -\left(L\frac{T^n-T_M}{T_M}q'(\phi^n)\frac{\phi^{n+1}-\phi^n}{\Delta t}, 1\right), \tag{3.14}$$

i.e.,

$$H^{n+1} - H^n = -\int_\Omega L\frac{T^n-T_M}{T_M}q'(\phi^n)(\phi^{n+1}-\phi^n)d\Omega. \tag{3.15}$$

Equation (3.11) is readily available if we sum up (3.13) and (3.15). □

Remark 1. *This energy law is consistent with the energy law* (3.4) *at the PDE level, but more dissipative. Unfortunately, H is not a norm of the solution (ϕ, T), and thus this discrete energy law can not serve as a condition for numerical stability.*

Chapter 4

Numerical Results

We use the finite element method to discretize (3.5) and (3.10) and the code is developed based on the deal.ii finite element library [25, 26]. The time discretization has first-order accuracy. Q2 finite elements on rectangular cells are used for both ϕ and T.

4.1 Isothermal Phase Transition

For simplicity, we first consider the isothermal phase transition, i.e., we only consider (3.1) (and semi-discrete weak form (3.5)) with $T = T_0$ being fixed, where T_0 is the initial temperature of the two-phase system.

The computational domain Ω is a unit square $[0, 1]^2$ with homogeneous natural boundary conditions: $\boldsymbol{n} \cdot \nabla\phi = 0$ and $\boldsymbol{n} \cdot \nabla T = 0$ on $\partial\Omega$. We consider an initially circular liquid drop surrounded by its solid phase. Due to symmetry, we only compute a quarter of the drop that is centered at the lower-left corner, as shown in Fig. 4.1. The computational parameters are listed in Table 4.1. The parameter λ (for the magnitude of mixing energy) can be obtained by $\lambda = 3\sqrt{2}\sigma\varepsilon$. The computational domain is partitioned into 128×128 square cells.

We use the following initial condition for ϕ:

$$\phi_0 = \frac{1}{2}\left(1 + \tanh\frac{d}{\sqrt{2}\varepsilon}\right), \tag{4.1}$$

where $d = R_0 - \sqrt{x^2 + y^2}$ and $R_0 = 0.5$ is the initial drop radius.

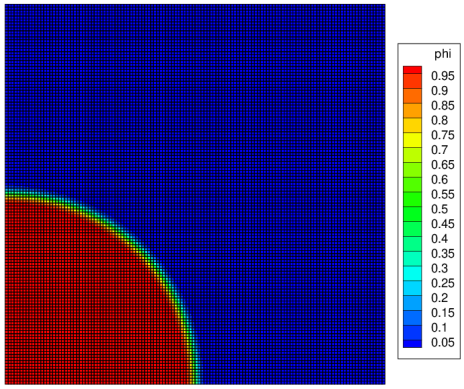

Figure 4.1: Initial interface and computational mesh.

Parameter	Symbol	Value
Melting temperature	T_M	1
Latent heat of fusion per unit volume	L	1
Mobility parameter	M_ϕ	1
Surface tension	σ	0.1
Interfacial thickness	ε	0.01
Heat capacity per unit volume	C_p	1
Thermal conductivity	k	0.1

Table 4.1: Parameters used for test case.

4.1.1 Time convergence

Although the convex-splitting-based scheme can achieve unconditional stability, it only has first order accuracy in time. In practice, we may still need to use very small time step Δt to achieve acceptable temporal accuracy. In this subsection, we will identify the range of Δt for a reasonable accuracy. Meanwhile, we will also verify the first-order accuracy of the scheme 3.5.

At a fixed temperature $T = T_0$, the propagation speed of the phase front is given by (2.39). For a drop with radius $R(t)$ at time t, this equation can be rewritten as

$$\frac{dR(t)}{dt} = -\mu_k \left(T_M - T_0 + T_M \frac{\sigma}{LR(t)} \right), \tag{4.2}$$

where $\mu_k = \frac{3\sqrt{2}\varepsilon ML}{T_M}$. This equation can be easily solved by the ordinary differential equation solver `ode45` in Matlab.

We take $T_0 = 0$ and test different Δt. We first compare the numerical results with the prediction of (4.2), as shown in Fig. 4.2. As Δt decreases, the numerical curve approaches the theoretical one. Roughly speaking, we need to take $\Delta t \leq 10^{-4}$ to obtain reasonable agreement.

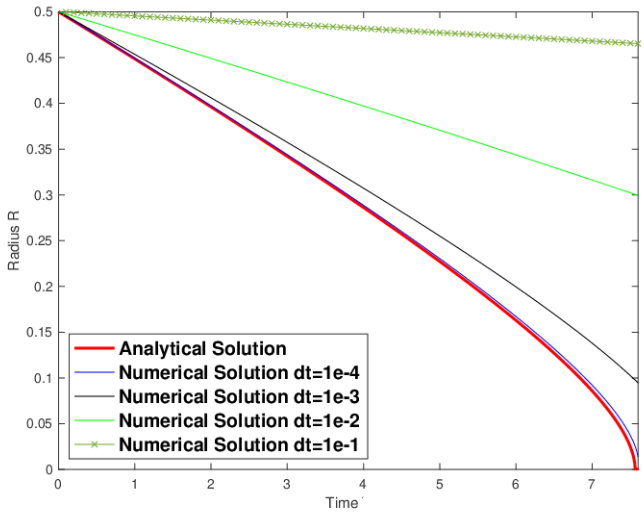

Figure 4.2: Comparison between the numerical solution of (3.5) and the analytical solution of (4.2).

It should be noted that there are some simplifications in the derivation of (2.39) and thus the solution of (4.2) is not exactly the solution of the partial differential equation (2.33). In order to perform convergence test, we have to use a different reference solution to compute the error. We use the numerical solution with $\Delta t = 10^{-6}$ as the reference solution. Since spatial order, which is expected to be 3 for the Q2 finite-element space, is much higher than the temporal order, we did not use a finer mesh when we computed the reference solution. We perform the simulations until $t = 1$ and compare the radial displacement of the interface. The initial drop radius is measured to be $R_0 = 0.500164$. For $\Delta t = 10^{-6}$ we have $R = 0.44882$ at $t = 1$ and thus displacement is $\Delta R = 5.13 \times 10^{-2}$. The result for different Δt are given in Table 4.2, where we can clearly see the first order convergence. Since $\Delta t = 1.25 \times 10^{-4}$ has roughly a relative error of 1%, we will take $\Delta t = 10^{-4}$ in all the following compuations.

4.1.2 Interface evolution at different T_0

Due to the Gibbs-Thomson effect, the actual melting temperature is predicted by (2.36). For our chosen parameters, we have

$$T_R = T_M + \frac{\sigma T_M}{R_0 L} = 1.2. \tag{4.3}$$

Δt	$R(t=1)$	ΔR	Error %	Order
1×10^{-3}	0.453594	4.65×10^{-2}	9.38	-
5×10^{-4}	0.451299	4.88×10^{-2}	4.87	0.94
2.5×10^{-4}	0.450065	5.01×10^{-2}	2.45	0.99
1.25×10^{-4}	0.449424	5.07×10^{-2}	1.19	1.04
6.26×10^{-5}	0.449098	5.11×10^{-2}	0.54	1.12

Table 4.2: Errors in interface displacement ΔR at $t = 1$.

Case 1: $T_0 = 1.2$

In this case $T_R = T_0$. Theoretically, the system is in equilibrium and the interface should remain fixed. We perform the simulation until $t = 40$. The snapshots of ϕ contours are given in Fig. 4.3 and the time history of drop radius is given in Fig. 4.4. Both figures indicate that the interface does stay stationary, which is consistent with the theoretical expectation.

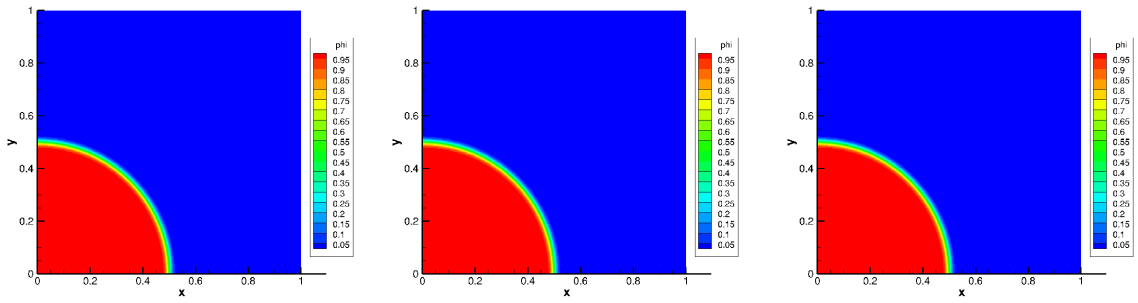

(a) Time=0 (b) Time=1 (c) Time=40

Figure 4.3: Snapshots of ϕ contours for isothermal phase transition at $T_0 = 1.2$.

Case II: $T_0 = 1$

In this test case, $T_0 < T_R$ and we expect the liquid to solidify, i.e., the drop shrinks. The results in Figs. 4.5 and 4.6 supports this expectation. Moreover, the drop radius agrees with the theoretical analysis.

Case III: $T_0 = 2$

In this case, we set T_0 higher than T_R. The ice is expect to melt and thus the drop expands. This is verified by Figs. 4.7 and 4.8.

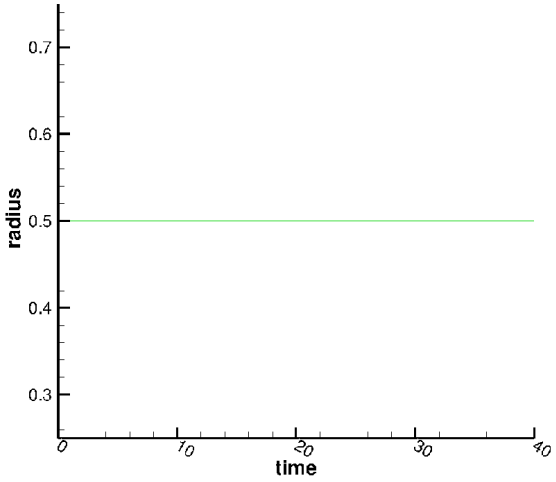

Figure 4.4: Evolution of drop radius for isothermal phase transition at $T_0 = 1.2$

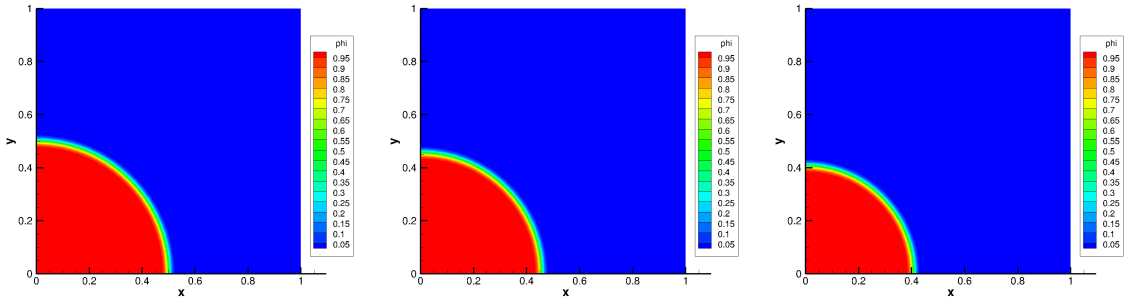

(a) Time=0 (b) Time=5 (c) Time=10

Figure 4.5: Snapshots of ϕ contours for isothermal phase transition at $T_0 = 1$.

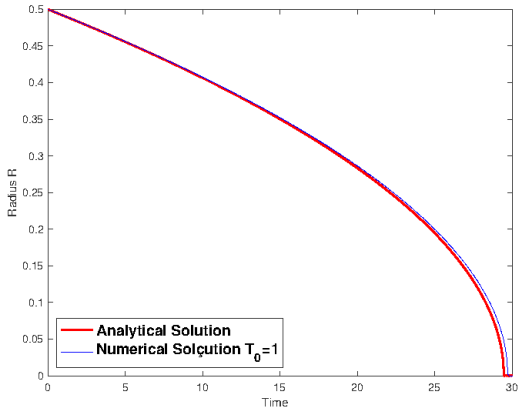

Figure 4.6: Evolution of drop radius for isothermal phase transition at $T_0 = 1$

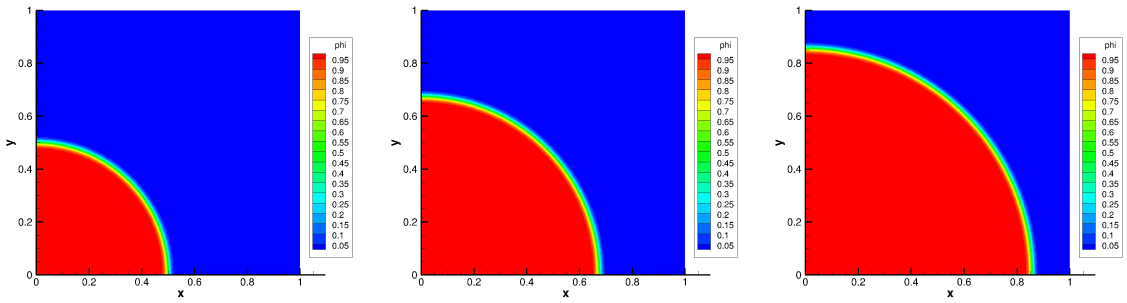

(a) Time=0 (b) Time=5 (c) Time=10

Figure 4.7: Snapshots of ϕ contours for isothermal phase transition at $T_0 = 2$.

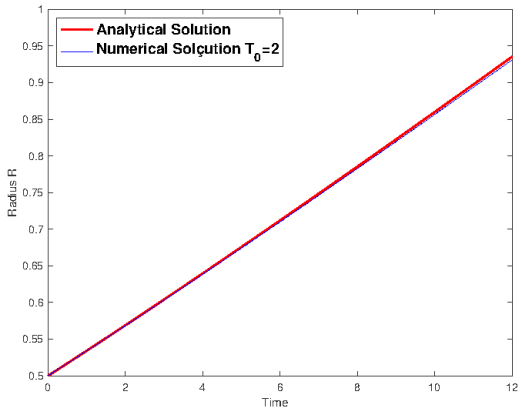

Figure 4.8: Evolution of drop radius for isothermal phase transition at $T_0 = 2$

4.2 Phase transition coupled with heat transfer

In this section we consider the semi-discrete weak form (3.5) and (3.10) for the coupled system (3.1) and (3.2). The computational setup is the same as in the previous section and the parameters are given in Table 4.1.

Solidification is an exothermic process. When a supercooled liquid solidifies, the latent heat of fusion is released, which raises the temperature of the mixture. This is known as recalescence. According to (2.39), the solidification process slows down and may even halt. A similar phenomenon occurs when a solid melts.

If we neglect heat conduction and assume that the released heat is completely used to heat up the material that undergoes phase transition, then the temperature rise is given by

$$\Delta T = L/C_p. \tag{4.4}$$

Solidification may come to a complete stop if $T_0 + \Delta T > T_R$, i.e., $T_0 \in [0.2, 1.2]$ for our chosen parameters. Similarly, melting may stop if $T_0 - \Delta T < T_R$, i.e., $T_0 \in [1.2, 2.2]$. The situation gets more complicated if heat conduction is considered, which may affect the local temperature at the phase front by diffusing away the heat.

We first consider $T_0 = 1$, under which the liquid solidifies first but may stop later due to recalescence. We test heat conductivities $k = 0.1$ and 10^{-4}. The drop radius is given in Fig. 4.9. First of all, when temperature change is considered, the drop shrinks slower than fixing $T = T_0$. Secondly, as k decreases, drop shrinks at a lower rate and may even stop shrinking.

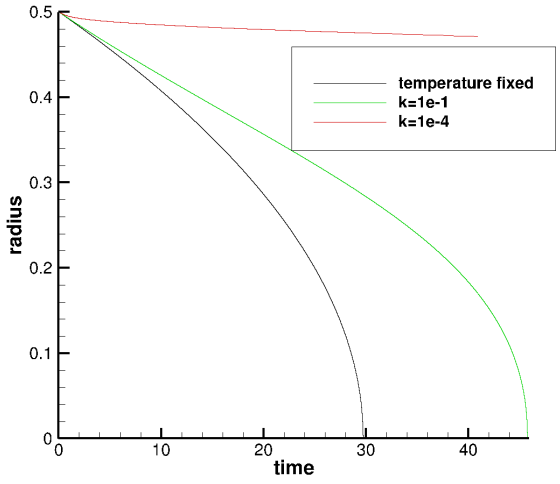

Figure 4.9: Evolution of drop radius for $T_0 = 1$.

The evolution of the temperature field for $k = 0.1$ is given in Fig. 4.10. It is obvious that the temperature in the whole domain increases as the solidification front advances (i.e., as

the drop shrinks), which slows down the rate of solidification. Detailed temperature fields at $t = 5$ are given in Fig. 4.11. At $k = 0.1$, the heat release at the solidification front can be quickly diffused into the bulk phases and the maximum temperature is only slightly above $T_0 = 1$. At $k = 10^{-4}$, the heat conductivity is so low that the temperature rise is focused at the diffuse interface. The maximum temperature is close to $T_R = 1.2$. As a result, the solidification front almost stops. In this case, the solidification rate is controlled by the slow heat transfer.

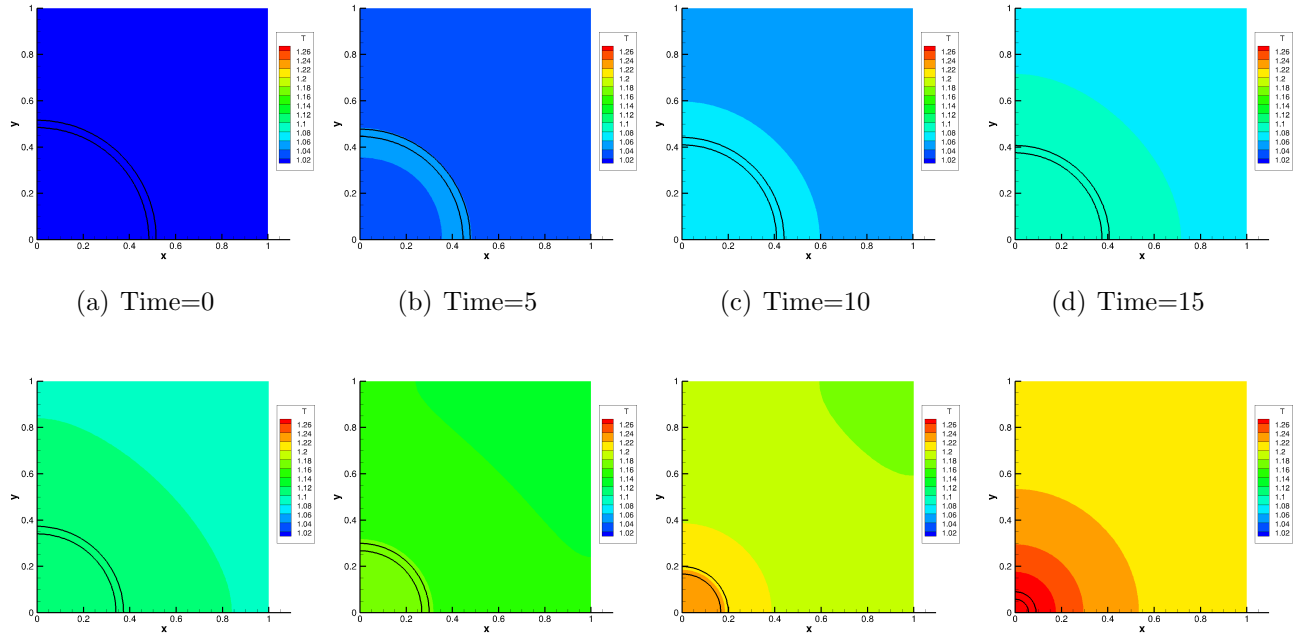

(a) Time=0 (b) Time=5 (c) Time=10 (d) Time=15

(e) Time=20 (f) Time=30 (g) Time=40 (h) Time=45

Figure 4.10: Snapshots of temperature contours for $T_0 = 1$ and $k = 0.1$. The solid lines are the contours of $\phi = 0.1$ and 0.9; same for the following contour plots.

We then consider $T_0 = 2$, under which the solid melts and consequently the drop expands. The drop radius is given in Fig. 4.12 and it is obvious that the consideration of temperature change slows down the drop expansion. The temperature field is given in Fig. 4.13. It is obvious that the temperature decreases as the drop expands, because the melting process is endothermic.

In summary, our model is able to capture recalescence, which slows down phase transition. In the extreme case of a very low heat conductivity, the temperature is raised (or decreased) to T_R at the phase front and the rate of phase transition almost drops to zero.

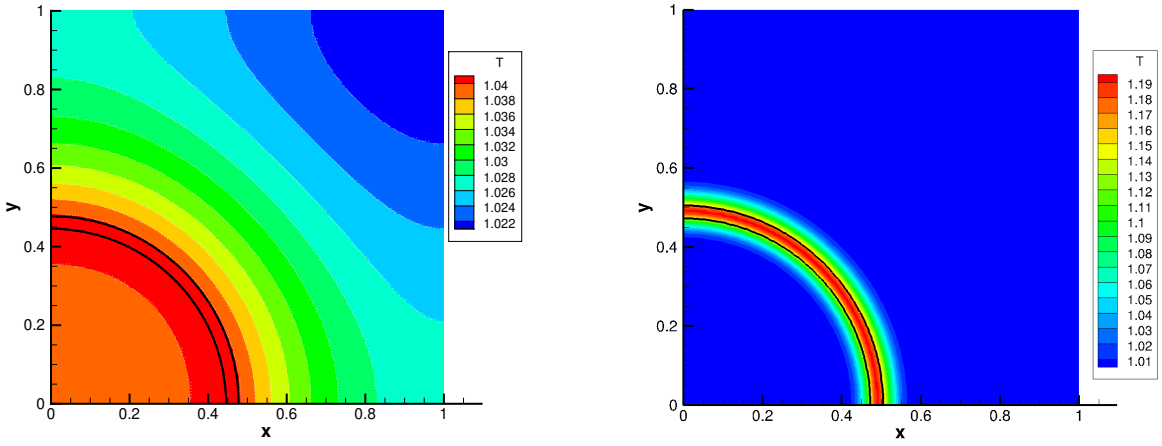

(a) $k = 0.1$ (b) $k = 10^{-4}$

Figure 4.11: Temperature contours for $T_0 = 1$ at $t = 5$.

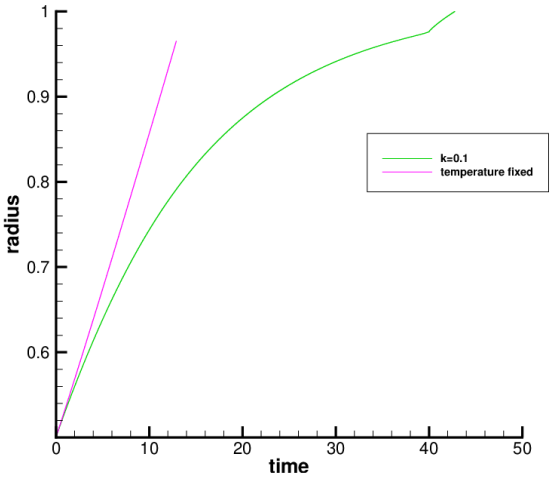

Figure 4.12: Expansion of drop at $T_0 = 2$.

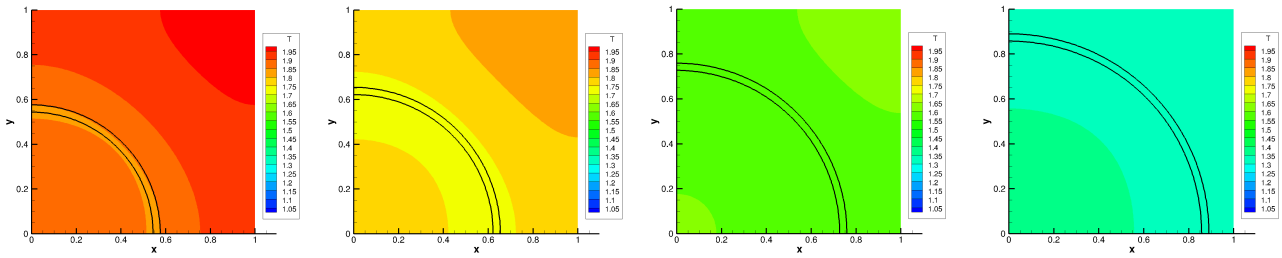

(a) Time=2 (b) Time=5 (c) Time=10 (d) Time=20

Figure 4.13: Snapshots of temperature contours for $T_0 = 2$ and $k = 0.1$

Chapter 5

Conclusions and Future Work

In this thesis, we have developed a coupled system of Allen-Chan equation and heat equation for the modeling of non-isothermal phase transition. A numerical scheme based on convex splitting is proposed for this equation system. A finite-element code based on deal.ii is developed, where the Q2 elements are used. The major results can be summarized as follows.

(i) The coupled system of Allen-Cahn and heat equations satisfies a dissipative energy law, and the numerical scheme satisfies a similar energy law at the discrete level.

(ii) For the isothermal case, the dynamic behavior to the interface is consistent with theoretical expectation. The numerical results successfully recover the Gibbs-Thomson and kinetic effects of solidification.

(iii) When heat production is considered, the phase transition is slowed down and recalescence is successfully captured by our simulations.

This work is still preliminary and we will consider the following extensions in the near future.

(i) Adaptive mesh refinement. The phase-field method requires a very fine mesh to resolve the diffuse interface. It is more economical to use an adaptive mesh that only refines at the interface rather than a uniformly fine mesh.

(ii) Anisotropic free energy. This is required to capture the dendritic solidification.

(iii) Consideration of variations in thermophysical properties and convection. Different phases may have very different thermophysical properties. For example, the density of ice is around 90% of that of water. As water solidifies, its volume expands and inevitably causes flow. The Navier-Stokes equations have to be added to account for flow.

(iv) Higher-order energy stable numerical schemes. The current scheme is only first-order and we have to use very small time steps to achieve good accuracy. We will consider some second-order energy stable schemes such as the Invariant Energy Quadratization (IEQ) approach [27] for the Allen-Cahn equation.

Chapter 6

Bibliography

[1] X. Yang and D. Han, Linearly first- and second-order, unconditionally energy stable schemes for the phase field crystal equation *J. Comput. Phys.*, vol. 330, pp. 1116–1134, 2017.

[2] J. Zhao, X. Yang, Y. Gong, and Q. Wang, A Novel Linear Second Order Unconditionally Energy stable Scheme for a Hydrodynamic Q-tensor Model of Liquid Crystals *Comput. Meth. Appl. Mech. Engrg.*, vol. 318, pp. 803–825, 2017.

[3] J. Zhao, X. Yang, J. Li, and Q. Wang, Energy stable numerical schemes for a hydrodynamic model of nematic liquid crystals *SIAM. J. Sci. Comput.*, vol. 38, pp. A3264–A3290, 2016.

[4] C. Wang and S. M. Wise, An energy stable and convergent finite-difference scheme for the modified phase field crystal equation *SIAM J. Numer. Anal.*, vol. 49, pp. 945–969, 2011.

[5] C. Chen and X. Yang, Efficient Numerical Scheme for a dendritic Solidification Phase Field model with melt convection *J. Comput. Phys.*, vol. 388, pp. 41–62, 2019.

[6] S.-L. Wang, R. F. Sekerka, A. A. Wheeler, B. T. Murray, S. Coriell, R. J. Braun, and G. McFadden, Thermodynamically-consistent phase-field models for solidification *Phys. D*, vol. 69, pp. 189–200, 1993.

[7] C. Beckermann, H.-J. Diepers, I. Steinbach, A. Karma, and X. Tong, Modeling melt convection in phase-field simulations of solidification *J. Comput. Phys.*, vol. 154, pp. 468–496, 1999.

[8] Y. Sun and C. Beckermann, Phase-field simulation of solidification with density change *Proc. IMECE04*, pp. 13–20, 2004.

[9] R. G. Larson, Constitutive equations for polymer melts and solutions *Butterworths-Heinemann*, 1988.

[10] R. Tönhardt and G. Amberg, Simulation of natural convection effects on succinonitrile crystals *Phys. Rev. E*, vol. 62, pp. 828–836, Jul 2000.

[11] K. W. Lipton J, Glicksman ME, Equiaxed dendrite growth in alloys at small supercooling *Mater. Sci. Eng.*, pp. 57–63, 1984.

[12] R. M. C. S. H.S. Furtadoa, A.T. Bernardesb, Numerical simulation of solute trapping phenomena using phase-field solidification model for dilute binary alloys *Mater. Res.*, p. 345–351, 2009.

[13] J. Shen and X. Yang, Numerical approximations of Allen-Cahn and Cahn-Hilliard equations *Discret. & Continuous Dyn. Syst. - A*, vol. 28, pp. 1669–1691, 2010.

[14] H. Yu and X. Yang, Numerical approximations for a phase-field moving contact line model with variable densities and viscosities *J. Comput. Phys.*, vol. 334, pp. 665 – 686, 2017.

[15] L. C. E. H. M. S. P. E. Souganidis, Phase transitions and generalized motion by mean curvature *Commun. on pure applied mathematics*, vol. 45, Issue9, pp. 1097–1123, 1992.

[16] D. Eyre, Unconditionally gradient stable time marching the cahn-hilliard equation *MRS Proc.*, p. 1686–1712, 1998.

[17] J. Shen and X. Yang, Numerical Approximations of Allen-Cahn and Cahn-Hilliard Equations *Disc. Conti. Dyn. Sys.-A*, vol. 28, pp. 1669–1691, 2010.

[18] W. J. Boettinger, J. A. Warren, C. Beckermann, and A. Karma, Phase-field simulation of solidification *Annu. Rev. Mater. Res.*, vol. 32, no. 1, pp. 163–194, 2002.

[19] M. A. Jaafar, D. R.Rousse, S. Gibout, and J.-P. Bedecarrats, A review of dendritic growth during solidification: Mathematical modeling and numerical simulations *Renew. Sustain. Energy Rev.*, vol. 74, pp. 1064 – 1079, 2017.

[20] A. Karma and W. Rappel, Phase-field model of dendritic sidebranching with thermal noise *Phys. Rev. E*, vol. 60, pp. 3614–3625, 1999.

[21] R. Hobayashi, Modeling and numerical simulations of dendritic crystal growth *Phys. D*, vol. 63, p. 410, 1993.

[22] C. Beckermann, H.-J. Diepers, I. Steinbach, A. Karma, and X. Tong, Modeling melt convection in phase-field simulations of solidification *J. Comput. Phys.*, vol. 154, no. 2, pp. 468 – 496, 1999.

[23] P. Yue, C. Zhou, J. J. Feng, C. F. Ollivier-Gooch, and H. H. Hu, Phase-field simulations of interfacial dynamics in viscoelastic fluids using finite elements with adaptive meshing *J. Comput. Phys.*, vol. 219, pp. 47–67, 2006.

[24] J. Brackbill, D. Kothe, and Z. CA, A continuum method for modeling surface tension *J. Comput. Phys.*, vol. 100, pp. 335–354, 1992.

[25] W. Bangerth, R. Hartmann, and G. Kanschat, deal.II – a general purpose object oriented finite element library *ACM Trans. Math. Softw.*, vol. 33, no. 4, pp. 24/1–24/27, 2007.

[26] G. Alzetta, D. Arndt, W. Bangerth, V. Boddu, B. Brands, D. Davydov, R. Gassmoeller, T. Heister, L. Heltai, K. Kormann, M. Kronbichler, M. Maier, J.-P. Pelteret, B. Turcksin, and D. Wells, The `deal.II` library, version 9.0 *J. Numer. Math.*, vol. 26, no. 4, pp. 173–183, 2018.

[27] C. Chen and X. Yang, Efficient numerical scheme for a dendritic solidification phase field model with melt convection *J. Comput. Phys.*, vol. 388, pp. 41 – 62, 2019.